

Theory of the sub-Sharvin charge transport in graphene disks

Adam Rycerz and Piotr Witkowski

Institute for Theoretical Physics, Jagiellonian University, Łojasiewicza 11, PL-30348 Kraków, Poland

(Dated: September 28, 2022)

Ballistic graphene samples in a multimode regime show the sub-Sharvin charge transport, characterized by the conductance reduced by a factor of $\pi/4$ comparing to standard Sharvin contacts in two-dimensional electron gas, and the shot-noise power enhanced up to $F \approx 1/8$ (with F the Fano factor) [Phys. Rev. B **104**, 165413 (2021)]. Here we consider the disk-shaped (Corbino) setup in graphene, with inner radius r_1 and outer radius r_2 , finding that the multimode conductance is slightly enhanced for any $r_1 < r_2$, reaching $(4 - \pi) \approx 0.8684$ of the Sharvin value for $r_1 \ll r_2$. At the same limit, the Fano factor is reduced, approaching $(9\pi - 28)/(12 - 3\pi) \approx 0.1065 < 1/8$. Closed-form approximating expressions for any r_1/r_2 ratio are derived supposing incoherent scattering of Dirac fermions on asymmetric double barrier and compared with exact numerical results following from the mode-matching method. Sub-Sharvin values are restored in the narrow-disk limit $r_1/r_2 \rightarrow 1$. For experimentally-accessible radii ratios $0.5 \leq r_1/r_2 \leq 0.8$ both the conductance and the Fano factor are noticeably closer to the values predicted for the $r_1 \ll r_2$ limit, yet still differ from standard Sharvin transport characteristics. The system behavior upon tuning the electrostatic potential barrier from a rectangular to parabolic shape is studied numerically, and the crossover from the sub-Sharvin to standard Sharvin transport regime is demonstrated. Implications for a finite section of the disk are also discussed.

I. INTRODUCTION

Several unique properties of graphene can be attributed to the fact that material characteristics of this form of carbon are determined by unusual properties of massless Dirac fermions in two dimensions [1–18]. In particular, chiral nature of effective quasiparticles and conical dispersion [1, 2] lead to half-integer sequence of quantum-Hall states [3–5] and quantized light absorption [6, 7]. The phenomenon of Klein tunneling [8] and transport via evanescent waves result in universal *dc* conductivity ($\sigma_0 = 4e^2/\pi h$, with the electron charge $-e$ and the Planck constant h) and *pseudodiffusive* shot noise power (quantified by the Fano factor $F = 1/3$) [9–12] in samples close to the charge-neutrality point. Even though thermal conductivity of graphene is dominated by phonons [13], and therefore only partly-related to the properties of Dirac electrons, some excess thermal conductance from these electrons [14], violating the Wiedemann-Franz law obeyed by the Schrödinger electrons, was detected [15]. Also, the presence of the valley degree of freedom affects several hallmarks of mesoscopic physics, including the conductance and spectral fluctuations [16–18].

Recently, it was shown using slightly different theoretical approaches [19–21] that the electrical conductance of a rectangular graphene sample away from the charge-neutrality point is reduced, while the Fano factor is amplified comparing to standard ballistic systems [22], namely

$$G = \frac{\pi}{4} G_{\text{Sharvin}}, \quad F = \frac{1}{8}, \quad (1)$$

with the Sharvin conductance $G_{\text{Sharvin}} = g_0 k_F W / \pi$ being the upper bound for the conductance of ballistic nanostructures [23, 24]. The conductance quantum is $g_0 = 4e^2/h$ due to the spin and valley degeneracies; the Fermi momentum k_F is tuned using the gate electrode such that $k_F^{-1} \ll \min(W, L)$, with W the sample width and L the sample length. Although the sample conductance is rather difficult to determine experimentally due to the resistances of contacts, existing experi-

ments report the Fano factor approaching $F \approx 0.10 \div 0.15$ [11, 12] away from the charge-neutrality point, being significantly greater than $F \approx 0$ expected for ballistic systems.

It is further found in Ref. [21] that the ballistic values of $G \approx G_{\text{Sharvin}}$ and $F \approx 0$ are gradually restored when the longitudinal potential barrier evolves from a rectangular towards a parabolic shape.

In the so-called *sub-Sharvin* transport regime, when k_F is approximately constant in the whole sample area (in other words, each potential jump in a contact region occur on a lengthscale $\Delta x \ll \lambda_F/2$, with λ_F being a typical Fermi wavelength in the sample area), transmission probability can be approximated by [21]

$$T \approx \cos \theta = \sqrt{1 - (k_y/k_F)^2}, \quad (2)$$

where θ denotes the direction of propagation in the central area (with respect to the longitudinal axis) and k_y is the transverse momentum component. Summing over possible values of $|k_y| \leq k_F$ in accordance with the Landauer-Büttiker formula [25, 26], one immediately obtains the values given in Eq. (1) provided that $k_F W \gg 1$ and $k_F L \gg 1$ [27].

Remarkably, the above-mentioned result is insensitive to the system aspect ratio (W/L) suggesting it may also be independent of the sample geometry. However, the idealized boundary conditions used in theoretical considerations usually lead to results which become comparable with the experiment starting from $W/L \gtrsim 20$, see Refs. [9, 11]. (For $W < L$, the conductance is suppressed, mainly due to the presence of edge disorder [28–31].) For these reasons, we consider here the edge-free Corbino geometry, for which the existing experimental [4, 5, 32] and theoretical [33–36] background allows to revisit the sub-Sharvin charge-transfer characteristics in search for the geometry- (in particular, the radii-ratio-) related effects which may be confirmed using existing devices. Main findings of the present work are summarized in Fig. 1.

The remaining parts of the paper are organized as follows. In Sec. II, we derive an approximation for the transmission

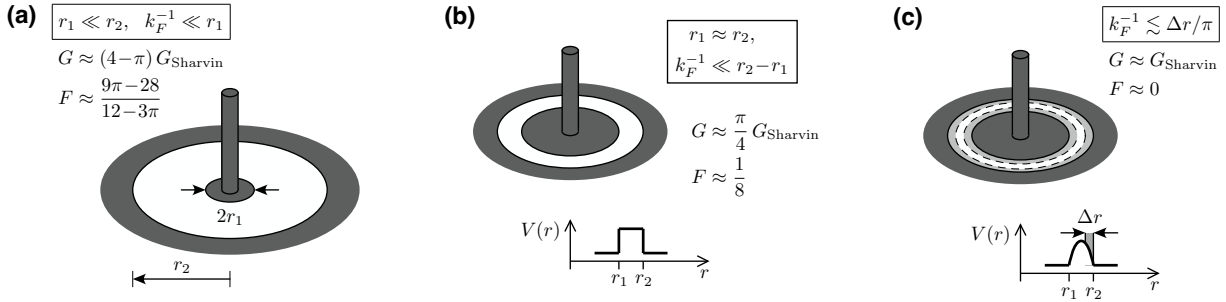


Figure 1: Outline of the results presented in the paper. For the Corbino disk, i.e., weakly-doped graphene annulus (white) attached to circular heavily-doped leads (dark), with the inner radius r_1 and the outer radius r_2 , the conductance (G) and Fano factor (F) approaches, in the multimode regime (with the Fermi wavenumber satisfying $k_F r_1 \gg 1$), the limiting values derived for different physical situations: (a) For a wide disk, $r_2 \gg r_1$, the values for incoherent scattering of Dirac fermions on a double barrier with perfect transmission on the outer potential step at the distance $r = r_2$ from the disk center, apply. (b) For a thin disk, $r_1 \approx r_2$, the values for incoherent scattering on a symmetric double barrier are restored. (c) If the rectangular potential barrier is replaced with a smooth one, with effective depth of a potential step Δr , the standard Sharvin transport characteristics show up for $k_F \Delta r \gtrsim \pi$.

through a doped Corbino disk in graphene and subsequent formulas for charge-transfer characteristics: the conductance and the Fano factor. Comparison with the exact numerical results from the mode-matching analysis is given in Sec. III. Next, in Sec. IV, we discuss the effects of tuning the potential barrier from a rectangular to a parabolic shape. The role of sample edges, modeled via the infinite-mass boundary conditions, is studied in Sec. V. The conclusions are given in Sec. VI.

II. APPROXIMATE CONDUCTANCE AND FANO FACTOR FOR GRAPHENE DISK

A. Scattering on straight interfaces

The reflection and transmission probabilities for the straight interface separating weakly- and heavily-doped regions in graphene [see Fig. 2(a)] can be written, in the limit of an infinite doping on one side, as functions of the incident angle θ

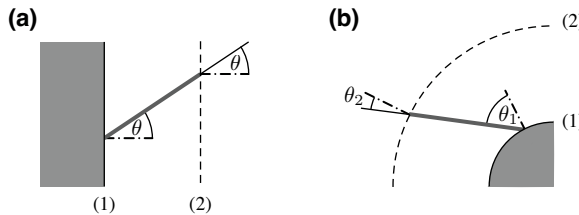


Figure 2: Propagation between scattering on interfaces (1) and (2) separating weakly doped [white area] and heavily doped [shadow area; omitted for interface (2) for clarity] regions in graphene (schematic). (a) The rectangular geometry. (b) The Corbino disk. Angular momentum conservation implies that incident angles for a particle satisfy $\theta_2 < \theta_1$ (if $\theta_1 > 0$) for the disk case. (Notice that thin solid lines behind the interface (2), visually elongating the trajectory mark with thick lines, are guide for the eye only; same applies to dash-dotted lines marking the normal to an interface.)

on the other (i.e., weakly-doped) side [10, 34], namely

$$R_1 = \frac{1 - \cos \theta}{1 + \cos \theta}, \quad T_1 = \frac{2 \cos \theta}{1 + \cos \theta}, \quad (3)$$

where $\cos \theta$ is related to the momentum component parallel to the interface (k_y) via the second equality in Eq. (2). In particular,

$$T_1 = \frac{2 \sqrt{1 - (k_y/k_F)^2}}{1 + \sqrt{1 - (k_y/k_F)^2}}. \quad (4)$$

For two interfaces in series, one can employ the double-contact formula [37] for the transmission

$$T = \frac{T_1 T_2}{1 + R_1 R_2 - 2\sqrt{R_1 R_2} \cos \phi}, \quad (5)$$

where T_2 and $R_2 = 1 - T_2$ are transmission and reflection probabilities for the second interface, and ϕ denotes the phase shift acquired during a single round-trip between the scatterers. Substituting $T_2 = T_1$ as given by Eq. (4) and $\phi = 2k_x L = 2\sqrt{k_F^2 - k_y^2} L$ for interfaces at a distance L , we obtain

$$T = \frac{1}{1 + (k_y/k_x)^2 \sin^2(k_x L)}. \quad (6)$$

The above holds true for propagating modes ($k_y \leq k_F$). For evanescent modes ($k_y > k_F$) one can obtain the analytic continuation by setting $k_x = i\sqrt{k_y^2 - k_F^2}$.

B. Landauer-Büttiker formalism

For a confined geometry, the quantization of k_y appears. For instance, if the infinite-mass confinement is assumed [38], we have $k_y = k_y^{(n)} \equiv \pi(n + \frac{1}{2})/W$ with $n = 0, 1, 2, \dots$ [39]. Substituting $k_y^{(n)}$ to Eq. (6) we obtain the transmission

probability for n -th normal mode T_n . Next, the conductance and the Fano factor follow by summing over the modes,

$$G = g_0 \sum_{n=0}^{N-1} T_n, \quad F = \frac{\sum_{n=0}^{N-1} T_n(1-T_n)}{\sum_{n=0}^{N-1} T_n}, \quad (7)$$

where $N = \lfloor WK/\pi \rfloor$ is the number of propagating modes in the leads for a finite doping (K denotes the Fermi momentum in the leads) considered further in this paper. The limit of infinite doping corresponds to $N \rightarrow \infty$ in Eq. (7).

Earlier in Ref. [21], we have argued that for high doping in the sample area, $k_F \gg W^{-1}$ and $k_F \gg L^{-1}$, the argument of sine in Eq. (6), i.e., $k_x L = \phi/2$, can be regarded as a random phase when summing contributions for consecutive n -s in Eq. (7). Also, the role of evanescent modes is negligible in such a range. In turn, T_n can be approximated by substituting $k_y = k_y^{(n)}$ to the rightmost formula in Eq. (2) for $k_y^{(n)} \leq k_F$, or by 0 for $k_y^{(n)} > k_F$. The corresponding formula for $(T_n)^2$ can be derived by averaging a square of Eq. (6) over ϕ , and reads

$$(T_n)^2 \approx \sqrt{1 - \left(\frac{k_y^{(n)}}{k_F}\right)^2} \left[1 - \frac{1}{2} \left(\frac{k_y^{(n)}}{k_F}\right)^2\right]. \quad (8)$$

Additionally, since $k_F \gg \Delta k_y = \pi/W$ being the transverse momentum quantum, the sums appearing in Eq. (7) can be replaced by integrals over $0 \leq k_y < k_F$, leading to the expressions for G and F given in Eq. (1).

Here, we point out that the above-mentioned results can also be obtained using the double-contact formula for incoherent transmission [37, 40], namely

$$\begin{aligned} \{T\}_{\text{incoh}} &= \frac{1}{2\pi} \int_{-\pi}^{\pi} d\phi \frac{T_1 T_2}{1 + R_1 R_2 - 2\sqrt{R_1 R_2} \cos \phi} \\ &= \frac{T_1 T_2}{1 - R_1 R_2} = \frac{T_1 T_2}{T_1 + T_2 - T_1 T_2}. \end{aligned} \quad (9)$$

Substituting $T_2 = T_1$ given by Eq. (4), we immediately obtain relevant formulas in Eqs. (1) and (2). Similarly, calculating

$$\begin{aligned} \{T^2\}_{\text{incoh}} &= \frac{1}{2\pi} \int_{-\pi}^{\pi} d\phi \left(\frac{T_1 T_2}{1 + R_1 R_2 - 2\sqrt{R_1 R_2} \cos \phi} \right)^2 \\ &= \frac{(T_1 T_2)^2 (1 + R_1 R_2)}{(1 - R_1 R_2)^3} \end{aligned} \quad (10)$$

brought us [for $T_2 = T_1$ given by Eq. (4), $R_{1(2)} = 1 - T_{1(2)}$, again] to Eq. (8) and the value of F given in Eq. (1). (Notice that evaluating incoherent square of the transmission probability in Eq. (10), later used to determine the shot-noise power, one need to calculate squared coherent probability first, and then average the result over a random phase.)

C. Implications for the Corbino disk

Although the double-contact formula cannot be directly applied to the Corbino disk [see Fig. 2(b)] Eqs. (9) and (10) give us a useful tool to generate approximate formulas for charge-transfer characteristics also in this case. Now, the angular momentum ($\hbar j$) is a conserved quantity for a particle traveling through the disk area. In turn, k_y in Eq. (4) needs to be replaced by j/r_1 , while an analogous expression for T_2 can be generated by substituting j/r_2 instead of k_y in Eq. (4). Using the last formula in Eq. (9) we obtain

$$\{T\}_{\text{incoh}} = \frac{2c_1 c_2}{c_1 + c_2}, \quad \text{with } c_{1(2)} = \sqrt{1 - \left(\frac{j}{r_{1(2)} k_F}\right)^2}, \quad (11)$$

being related to incident angles in Fig. 2(b) via $c_{1(2)} = \cos \theta_{1(2)}$. Similarly, from Eq. (10) we get

$$\{T^2\}_{\text{incoh}} = 4 \frac{c_1^2 c_2^2 (1 + c_1 c_2)}{(c_1 + c_2)^3}. \quad (12)$$

In order to calculate measurable quantities we employ Eq. (7) approximating (for $k_F \gg 1/r_1$) sums by integrals over a dimensionless $u = j/(r_1 k_F)$, in the interval $-1 \leq u \leq 1$. For the conductance, we get

$$G = 2g_0 r_1 k_F \int_0^1 du \{T\}_{\text{incoh}} = G_{\text{Sharvin}} \times \frac{(2a + \frac{1}{a}) \arcsin a + 3\sqrt{1-a^2} - \frac{\pi}{2}(a^2 + 2)}{1-a^2}, \quad (13)$$

where we have used parity of Eq. (11) upon $j \leftrightarrow -j$ to shrink the integration range to $0 \leq u \leq 1$, introduced $G_{\text{Sharvin}} = 2g_0 r_1 k_F$ being the Sharvin conductance for a disk, and defined the inverse radii ratio $a = r_1/r_2 < 1$. The Fano factor now reads

$$\begin{aligned} F &= 1 - \int_0^1 du \{T^2\}_{\text{incoh}} / \left(\int_0^1 du \{T\}_{\text{incoh}} \right) \\ &= \frac{2a\sqrt{1-a^2}(53 + 279a^2 + 88a^4) - 3\pi a(12 + 82a^2 + 45a^4 + a^6) + 6(1 + 45a^2 + 82a^4 + 12a^6) \arcsin a}{6(1-a^2)^2 [\pi a(a^2+2) - 6a\sqrt{1-a^2} - 2(2a^2+1) \arcsin a]}. \end{aligned} \quad (14)$$

Asymptotic forms of Eqs. (13) and (14) are the following

$$G \simeq \frac{\pi}{4} G_{\text{Sharvin}}, \quad F \simeq \frac{1}{8}, \quad \text{for } a \rightarrow 1, \quad (15)$$

and

$$G \simeq (4-\pi) G_{\text{Sharvin}}, \quad F \simeq \frac{9\pi-28}{12-3\pi}, \quad \text{for } a \rightarrow 0. \quad (16)$$

Formulas in Eq. (15) refer to the thin-disk limit ($r_1 \approx r_2$) and can be easily obtained by setting $c_2 \approx c_1$ in Eqs. (11) and (12) and repeating the subsequent steps. Similarly, Eq. (16) describes the wide-disk limit ($r_2 \gg r_1$), and can be obtained after setting $c_2 \approx 1$ (being equivalent to $T_2 \approx 1$ describing a perfect transmission for normal incidence) in Eqs. (11) and (12). Therefore, in the $r_2 \gg r_1$ limit the role of the outer interface (at $r = r_2$) is suppressed, and transport properties of the system are governed by scattering of Dirac fermions on a single potential step at the inner disk edge, at $r = r_1$.

III. EXACT SOLUTION FOR THE DISK

A. Mode-matching for the Dirac equation

The analysis starts from the Dirac equation for a single valley (K), which can be written as

$$[v_F \mathbf{p} \cdot \boldsymbol{\sigma} + V(r)] \Psi = E \Psi, \quad (17)$$

where $v_F = \sqrt{3} t_0 a / (2\hbar) \approx 10^6$ m/s is the energy-independent Fermi velocity in graphene (with $t_0 = 2.7$ eV the nearest-neighbor hopping integral and $a = 0.246$ the lattice parameter), $\mathbf{p} = (p_x, p_y)$ is the in-plane momentum operator with $p_j = -i\hbar\partial_j$, and $\boldsymbol{\sigma} = (\sigma_x, \sigma_y)$ with σ_j being the Pauli matrices. Taking the wavefunction in polar coordinates in a form $\Psi_j(r, \varphi) = e^{i(j-1/2)\varphi} (\chi_a, \chi_b e^{i\varphi})^T$, with $j = \pm 1/2, \pm 3/2, \dots$ the total angular-momentum quantum number, brought us to the system of ordinary differential equations for the spinor components

$$\chi'_a = \frac{j - 1/2}{r} \chi_a + i \frac{E - V(r)}{\hbar v_F} \chi_b, \quad (18)$$

$$\chi'_b = i \frac{E - V(r)}{\hbar v_F} \chi_a - \frac{j + 1/2}{r} \chi_b. \quad (19)$$

In this section, our discussion is limited to a piecewise-constant potential energy $V(r)$, earlier considered in Ref. [34]. For the electron-doping case, $E > V(r)$, solutions for the incoming (i.e., propagating from $r = 0$) and outgoing (propagating from $r = \infty$) waves are given, up to the normalization, by

$$\chi_j^{\text{in}} = \begin{pmatrix} H_{j-1/2}^{(2)}(kr) \\ iH_{j+1/2}^{(2)}(kr) \end{pmatrix}, \quad \chi_j^{\text{out}} = \begin{pmatrix} H_{j-1/2}^{(1)}(kr) \\ iH_{j+1/2}^{(1)}(kr) \end{pmatrix}, \quad (20)$$

where $H_\nu^{(1,2)}(\rho)$ is the Hankel function of the (first, second) kind, and $k = |E - V(r)| / (\hbar v_F)$. For the disk area, we have $V(r) = 0$, and the solution can be represented as

$$\chi_j^{(d)} = A_j \chi_j^{\text{in}}(k_F r) + B_j \chi_j^{\text{out}}(k_F r), \quad r_1 < r < r_2, \quad (21)$$

where A_j and B_j are arbitrary constants, and the Fermi wavenumber $k_F = |E| / (\hbar v_F)$. For the hole doping case, $E < U(r)$, the wavefunctions are replaced by $\tilde{\chi}_j^{\text{in(out)}} = [\chi_j^{\text{in(out)}}]^*$, using the relation $H_\nu^{(2)} = [H_\nu^{(1)}]^*$.

Heavily-doped graphene leads are usually modeled by taking the limit of $V(r) = V_0 \rightarrow \pm \infty$ for $r < r_1$ or $r > r_2$. The corresponding wavefunctions simplify to

$$\chi_j^{(1)} = \frac{e^{\pm i K r}}{\sqrt{r}} \begin{pmatrix} 1 \\ 1 \end{pmatrix} + r_j \frac{e^{\mp i K r}}{\sqrt{r}} \begin{pmatrix} 1 \\ -1 \end{pmatrix}, \quad r < r_1, \quad (22)$$

$$\chi_j^{(2)} = t_j \frac{e^{\pm i K r}}{\sqrt{r}} \begin{pmatrix} 1 \\ 1 \end{pmatrix}, \quad r > r_2, \quad (23)$$

with the reflection (and transmission) amplitudes r_j (and t_j) and $K = |E - V_0| / (\hbar v_F) \rightarrow \infty$.

Solving the mode-matching conditions, $\chi_j^{(1)}(r_1) = \chi_j^{(d)}(r_1)$ and $\chi_j^{(d)}(r_2) = \chi_j^{(2)}(r_2)$, we find the transmission probability for j -th mode

$$T_j = |t_j|^2 = \frac{16}{\pi^2 k^2 r_1 r_2} \frac{1}{[\mathfrak{D}_j^{(+)}]^2 + [\mathfrak{D}_j^{(-)}]^2}, \quad (24)$$

with

$$\mathfrak{D}_j^{(\pm)} = \text{Im} \left[H_{j-1/2}^{(1)}(kr_1) H_{j\mp 1/2}^{(2)}(kr_2) \right. \\ \left. \pm H_{j+1/2}^{(1)}(kr_1) H_{j\pm 1/2}^{(2)}(kr_2) \right]. \quad (25)$$

The result given by Eqs. (24) and (25) corresponds to rectangular shape and infinite height of the potential barrier $V(r)$. Other potential barriers are considered in Sec. IV.

B. Conductance and Fano factor

Numerical values of the conductance and the Fano factor, obtained for the two systems for which exact expressions for transmission probabilities T_n (or T_j) are available, are presented in Figs. 3 and 4 [41]. For rectangular samples with infinite-mass confinement, we simply took the limit of $N \rightarrow \infty$ in Eq. (7) numerically. For disks, T_n -s in Eq. (7) are replaced with T_j -s given by Eqs. (24) and (25), and the summations are performed for $-\infty < j < \infty$, with j being half-odd integer.

In Fig. 3(a), the conductance spectra for selected systems are compared with the asymptotic formulas given in Eqs. (15) and (16). Since the limit of an infinite rectangular barrier is considered, there are only two dimensionless parameters relevant: the radii (or aspect) ratio r_1/r_2 (or W/L) and the expected (dimensionless) Sharvin conductance $G_{\text{Sharvin}}/g_0 = 2k_F r_1$ (or $= k_F W/\pi$). In order to compare the results for different geometries, we further adjust the aspect ratio for rectangles such that the zero-energy conductance $G = (4/\pi)g_0 W/L$ is the same as for a given disk, namely: $W/L = 2\pi / \log(r_2/r_1)$, with $r_2/r_1 = 2$ and 1.25. The last relation can be easily derived by taking the zero-energy limit in Eq. (24), $T_j(k \rightarrow 0) = 4 / [(r_2/r_1)^j + (r_1/r_2)^j]^2$, and approximating the sum over j by an integral [42].

It is easy to see that the conductance spectra for rectangular samples [see thick solid lines in Figs. 3(a) and 3(b)] closely follow the sub-Sharvin formula $(\pi/4) G_{\text{Sharvin}}$ soon

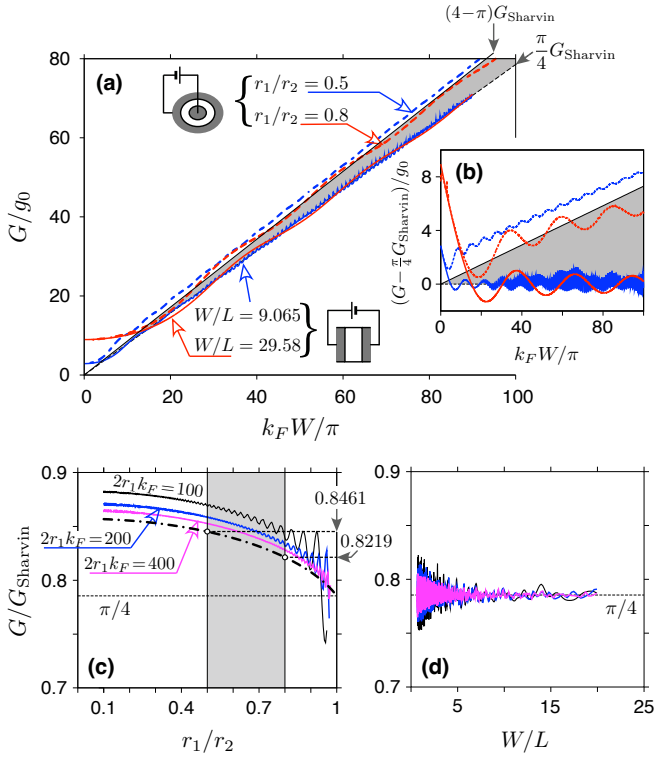


Figure 3: (a) Conductance as a function of the Fermi momentum for Corbino disks with the radii ratios $r_1/r_2 = 0.5$ and 0.8 (thick dashed lines) and for rectangular graphene samples (thick solid lines) with width-to-length ratios adjusted to match the zero-energy conductance, i.e., $W/L = 2\pi/\log(r_2/r_1)$, and specified for each line. Both types of systems are shown schematically. (b) The excess conductance above the sub-Sharvin value $(\pi/4)G_{\text{Sharvin}}$, with $G_{\text{Sharvin}} = g_0k_W/\pi$ (for the disks, we set $W = 2\pi r_1$). The conductance quantum is $g_0 = 4e^2/h$. (c) The conductance reduction as a function of the radii ratio for disks at fixed values of $G_{\text{Sharvin}}/g_0 = 2r_1k_F = 100, 200$, and 400 (specified for each solid line). Dash-dotted line marks the approximating formula given by Eq. (13); the numerical values for $r_1/r_2 = 0.5$ and 0.8 are indicated with open symbols and specified up to four decimal places. (d) The conductance reduction as a function of the aspect ratio for rectangles with same values of $G_{\text{Sharvin}}/g_0 = k_F W/\pi$ as in (c). Thin dashed lines in (a)–(d) mark the sub-Sharvin value $(\pi/4)G_{\text{Sharvin}}$. Thin solid lines in (a), (b) depict the asymptotic conductance for $r_1/r_2 \rightarrow 0$, being equal to $(4 - \pi)G_{\text{Sharvin}}$.

after the condition $k_F \gtrsim L^{-1}$ (i.e., the ballistic transport prevails over the pseudodiffusive transport) is satisfied. In contrast, the conductance spectra for disks [see thick dashed lines in Figs. 3(a) and 3(b)] slowly approach the upper limit of $(4 - \pi)G_{\text{Sharvin}}$ corresponding to $r_2 \gg r_1$. In fact, for the range of $2r_1k_F \leq 100$ used in Figs. 3(a) and 3(b), the values of $G < (4 - \pi)G_{\text{Sharvin}}$ can be noticed only for the case of $r_1/r_2 = 0.8$.

Results for higher values of $2r_1k_F$ are displayed, versus the radii ratio, in Fig. 3(c). It becomes clear now that the values following from approximating Eq. (13) for incoherent transmission [see black dash-dotted line] are approached by exact numerical results [solid lines] for any r_1/r_2 . However,

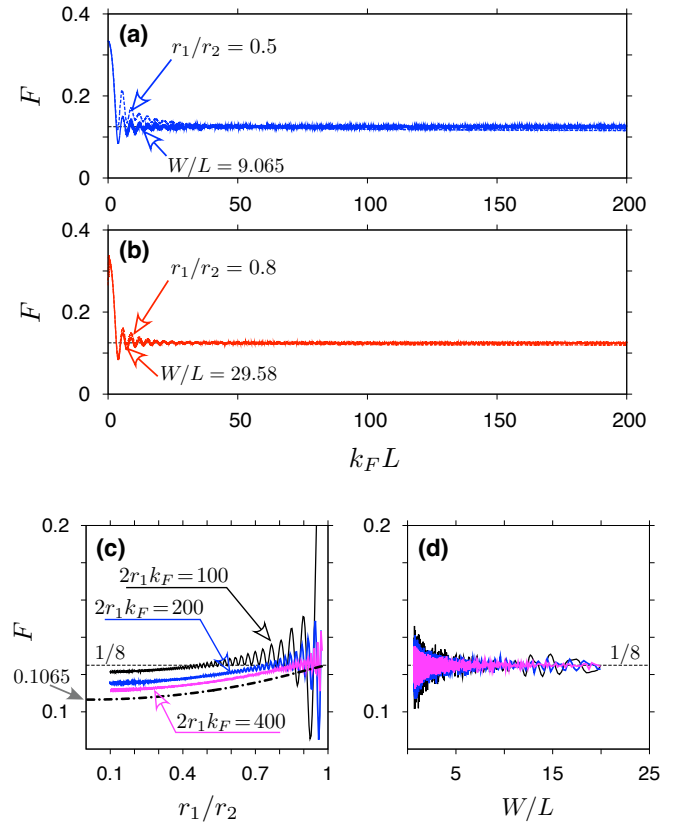


Figure 4: (a,b) Fano factor as a function of the Fermi momentum for same systems as in Figs. 3(a), 3(b). The radii ratio (or aspect ratio) is specified for each line. The sample length for disks is defined as $L = r_2 - r_1$. (c) Fano factor as a function of the radii ratio for disks and (d) as a function of the radii ratio for rectangles with same values of G_{Sharvin}/g_0 as used in Figs. 3(c) and 3(d). Dash-dotted line in (c) marks the approximating formula given by Eq. (14); the limiting value for $r_1/r_2 \rightarrow 0$ is specified up to four decimal places. Thin dashed lines in (a)–(d) mark the sub-Sharvin value of $F = 1/8$.

the convergence is noticeably slower than for rectangular samples, see Fig. 3(d). In physical units, the inner disk diameter of $2r_1 = 1000$ nm and the maximal Fermi energy of $|E| = 0.3$ eV (already reported for some graphene-hBN heterostructures, see Ref. [43]) correspond to $2r_1k_F \approx 522$, allowing us to expect that the values of $(4 - \pi) > G/G_{\text{Sharvin}} > \pi/4$ should be observable in graphene disks with moderate radii ratios $0.5 \leq r_1/r_2 \leq 0.8$.

Values of the shot-noise power for the same systems are presented in Fig. 4. This time, we display the Fano factor as a function of $k_F L$ (with $L = r_2 - r_1$ for disks) in order to visualize quasiperiodic oscillations of the Fabry-Pérot type, which are well-pronounced for both rectangular and disk-shaped samples with different aspect (or radii) ratios, see Figs. 4(a) and 4(b). Similarly as for the conductance, the Fano factor for rectangular samples [solid lines] shows fast convergence, with growing k_F , to the sub-Sharvin value of $F = 1/8$. For disks, the convergence is slower, and the limiting value for large k_F is significantly lower than $1/8$ [dashed lines].

Again, plotting the Fano factor for several fixed $2r_1k_F$ and

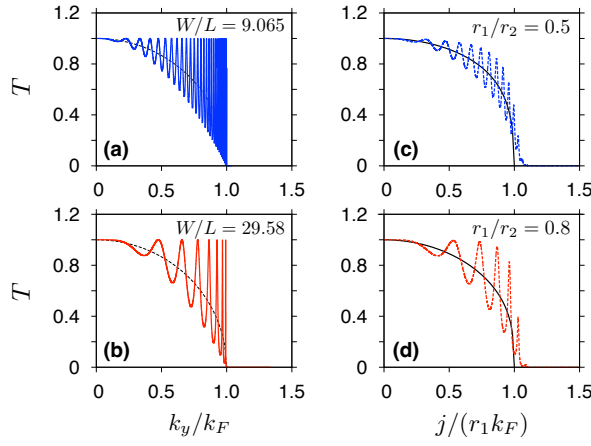


Figure 5: Transmission probability as a function of the transverse momentum for rectangular samples (a,b) or the total angular momentum for disks (c,d). The Fermi momentum is fixed such that $k_F L = r_1 k_F = 100$ (a,c) or $k_F L = (r_2 - r_1)k_F = 25$ (b,d). Remaining system parameters (specified at each panel) are same as in Figs. 4(a) and 4(b). Thin dashed lines in (a) and (b) mark Eq. (2); solid lines in (c) and (d) mark Eq. (11).

varying r_1/r_2 [see Fig. 4(c)], allows us to notice an apparent convergence of exact numerical results [solid lines] to predictions following from Eq. (14) [dash-dotted line]. Also, the above-mentioned convergence is noticeably slower for disks than for rectangular samples [see Fig. 4(d)].

For better understanding of the effects described in this section we plot, in Fig. 5, transmission probabilities given by Eq. (6) for rectangles, or by Eqs. (24) and (25) for disks, as functions of k_y/k_F or $j/(r_1 k_F)$ (respectively) at a fixed k_F . It is worth to point out, that Eqs. (24) and (25) are valid for any fractional value of j ; physically, other than half-odd integer j -s may appear in the presence of magnetic flux piercing the inner electrode, see Ref. [44].

Remarkably, transmission probability for evanescent modes, with $j/r_1 > k_F$, decays (with growing j) significantly slower for disks [see Figs. 5(c) and 5(d)] than for rectangular samples, for which we immediately have $T \approx 0$ if $k_y > k_F$ [see Figs. 5(a) and 5(b)]. This is the reason, for which charge-transfer characteristics obtained via Eq. (7) for disks generically show slower convergence (with growing k_F) to the predictions for incoherent transmission presented in Sec. II than it can be observed in corresponding data for rectangles.

IV. SMOOTH POTENTIAL BARRIERS

A. Mode-matching for smooth potentials

For the sake of completeness, we also revisit, in this section, the effects of smooth potential barriers, earlier considered for the rectangular geometry [21]. For the Corbino disk, key steps of the reasoning remain similar as presented in Sec. IIIA. However, the electrostatic potential energy in Eqs. (18) and (19) is now replaced by

$$V(r) = -V_0 \times \begin{cases} |(r - r_c)/r_0|^m & \text{if } |r - r_c| \leq r_0, \\ 1 & \text{if } |r - r_c| > r_0, \end{cases} \quad (26)$$

where $r_c = (r_1 + r_2)/2$ and $r_0 = (r_2 - r_1)/2$. Changing the value of m tunes the potential from parabolic shape ($m = 2$) to rectangular shape ($m \rightarrow \infty$), see Fig. 6.

Since $V(r) = -V_0$ for $r < r_1$ and $r > r_2$, solutions for the leads given by Eq. (20) remain unchanged. This time, we do not take the limit of $V_0 \rightarrow \infty$; instead, $V_0 = t_0/2 = 1.35$ eV (being close the values appearing in first-principle calculations [45, 46]) is considered in subsequent numerical examples. In turn, wavefunctions in the leads can now be written as follows

$$\chi_j^{(1)} = \chi_j^{\text{in}} + r_j \chi_j^{\text{out}}, \quad r < r_1, \quad (27)$$

$$\chi_j^{(2)} = t_j \chi_j^{\text{in}}, \quad r > r_2, \quad (28)$$

where χ_j^{in} , χ_j^{out} are given by Eq. (20) with $k \equiv k_0 = |E + V_0|/(\hbar v_F)$ [47] and r_j (t_j) denotes the reflection (transmission) amplitudes.

In the disk area, $r_1 < r < r_2$, $V(r)$ given by Eq. (26) is no longer piecewise-constant, and Eqs. (18) and (19) need to be integrated numerically for $j = \pm\frac{1}{2}, \pm\frac{3}{2}, \dots$ [48]. The resulting wavefunction takes a form

$$\chi_j^{(d)} = A \chi_j^{\text{I}} + B \chi_j^{\text{II}}, \quad (29)$$

where χ_j^{I} , χ_j^{II} denote the two linearly independent solutions, which we obtained numerically by solving the relevant equations assuming two different initial conditions $\chi_j^{\text{I,II}}|_{r=r_1} = (1, \pm 1)^T$, and A , B are arbitrary complex coefficients.

The matching conditions for $r = r_1$ and $r = r_2$ brought us to the linear system of equations for A , B , r_j , and t_j ,

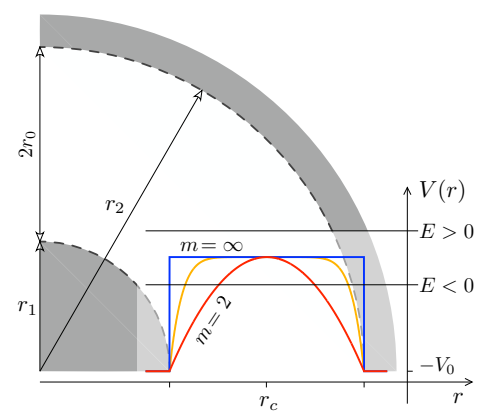


Figure 6: Electrostatic potential profiles given by Eq. (26) with $m = 2, 8$ and $m = \infty$ (i.e., the rectangular barrier). The Fermi energy E is defined with respect to the top of a barrier. $E > 0$ corresponds to unipolar n-n doping in the device; for $E < 0$, circular n-p-n structure is formed. Arcs with the radii r_1 and r_2 (dashed lines) mark the interfaces between the disk area [$r_1 < r < r_2$; white area] and contact regions [$r < r_1$ or $r > r_2$; shaded areas].

$$\begin{bmatrix} \chi_{j,a}^{\text{out}}(r_1) & -\chi_{j,a}^{\text{I}}(r_1) & -\chi_{j,a}^{\text{II}}(r_1) & 0 \\ \chi_{j,b}^{\text{out}}(r_1) & -\chi_{j,b}^{\text{I}}(r_1) & -\chi_{j,b}^{\text{II}}(r_1) & 0 \\ 0 & -\chi_a^{\text{I}}(r_2) & -\chi_{j,a}^{\text{II}}(r_2) & \chi_{j,a}^{\text{in}}(r_2) \\ 0 & -\chi_b^{\text{I}}(r_2) & -\chi_{j,b}^{\text{II}}(r_2) & \chi_{j,b}^{\text{in}}(r_2) \end{bmatrix} \begin{bmatrix} r_j \\ A \\ B \\ t_j \end{bmatrix} = \begin{bmatrix} -\chi_{j,a}^{\text{in}}(r_1) \\ -\chi_{j,b}^{\text{in}}(r_1) \\ 0 \\ 0 \end{bmatrix}, \quad (30)$$

where we have explicitly written the spinor components of relevant wavefunctions appearing on right-hand sides of Eqs. (27), (28), and (29). Since linear systems of the form given by Eq. (30) for different j -s are decoupled, numerous software packages can be employed to find their solutions up to a machine precision [49].

B. Sharvin conductance

Before presenting the numerical results obtained by finding the transmission probabilities $T_j = |t_j|^2$ from Eq. (30), we first comment how to define the Sharvin conductance for a disk-shaped system subjected to the electrostatic potential $V(r)$ given by Eq. (26). In such a case, we simply look for the minimal number of propagating modes in the disk area, writing

$$G_{\text{Sharvin}}^{(m)} = 2g_0 \min_{r_1 \leq r \leq r_2} [rk_F(r)], \quad (31)$$

where

$$k_F(r) = \frac{|E - V(r)|}{\hbar v_F}, \quad (32)$$

and the index m in Eq. (31) is the exponent defining $V(r)$. The Fermi wavenumber $k_F(r)$ is now position-dependent; hereinafter, using a simplified symbol (k_F) we always refer to $k_F(r_c) = |E|/(\hbar v_F)$.

For general values of r_1 , r_2 , and m , the minimum in Eq. (31) needs to be determined numerically. In the limit of $m \rightarrow \infty$, the minimum corresponds to $r_{\min} = r_1$ and we get

$$G_{\text{Sharvin}}^{(\infty)} = 2g_0 r_1 k_F, \quad (33)$$

restoring the formula for a rectangular barrier introduced in Eq. (13). For $m = 2$ (parabolic barrier) and $0 \leq E \ll V_0$, one can easily find that $r_{\min} \approx r_c$ [50], and that the following approximation

$$G_{\text{Sharvin}}^{(2)} \approx 2g_0 r_c k_F = (r_c/r_1) G_{\text{Sharvin}}^{(\infty)} \quad (34)$$

should be sufficient for typical, experimentally-accessible, values of r_1/r_2 and E .

C. Numerical results

In Fig. 7, we display transmission probabilities for systems with $r_1 = 800$ nm and two different values of $r_2 = 1600$ nm

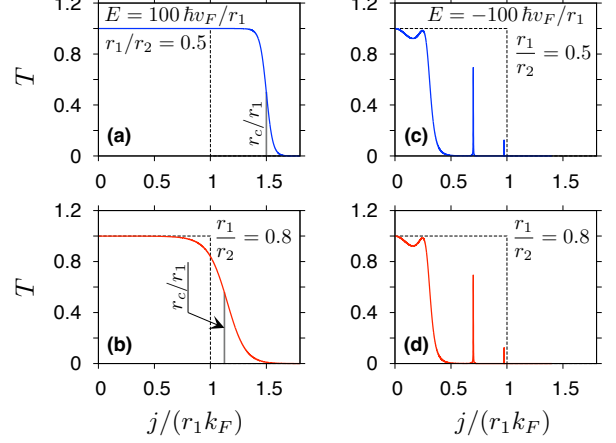


Figure 7: Transmission probability versus angular momentum for disks with parabolic potential barrier given by Eq. (26) with $m = 2$. The scattering energy is fixed at $E = 100 \hbar v_F/r_1$ (a,b) or $E = -100 \hbar v_F/r_1$ (c,d). The radii ratio is specified at each panel. The remaining parameters are $r_1 = 800$ nm and $V_0 = 1.35$ eV. Dashed lines depict the step functions $T_j = \Theta(k_F - |j|/r_1)$, with $k_F \equiv k_F(r_c) = |E|/(\hbar v_F)$ [see Eq. (32)]. Vertical lines in (a,b) show the ratio $r_c/r_1 = 1.5$ (a) or 1.125 (b).

and 1000 nm, corresponding to $r_1/r_2 = 0.5$ and 0.8 , as functions of j . (Fractional, i.e., other than half-odd integer values of j in Eq. (30) have no physical meaning here and are considered for plotting purposes only.) The parabolic barrier ($m = 2$) is considered in all cases. The Fermi energy is fixed at $E = 100 \hbar v_F/r_1$ or at $E = -100 \hbar v_F/r_1$, corresponding to $E \approx \pm 72$ meV in the physical units.

For $E > 0$ [see Figs. 7(a) and 7(b)], transmission essentially shows a familiar switching behavior [51], with $T \approx 1$ for $j/r_c < k_F$ and $T \approx 0$ for $j/r_c > k_F$. Notice that, comparing to the case of a rectangular barrier discussed in Sec. IIIB [see Figs. 5(c) and 5(d)], r_c now plays a role similar to r_1 , coinciding with a prediction given in Eq. (34). For $E < 0$, see Figs. 7(c) and 7(d), the presence of two circular p-n junctions [positioned at $r = r_*$ such that $V(r_*) = E$, see Fig. 6] significantly reduces the transmission for almost any j .

Numerical results for the conductance and Fano factor, obtained by summing over the modes [see Eq. (7)] with half-odd integer j , are presented in Figs. 8 and 9. We consider the radii ratio of $r_1/r_2 = 0.8$ now, in order to find out whether (or not) the modifications to sub-Sharvin charge-transfer characteristics, described in Secs. II and III, are still significant in such a relatively thin disk subjected to smooth potential barrier of a finite height.

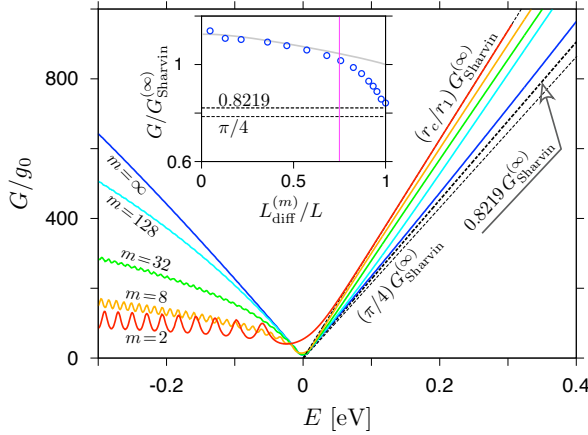


Figure 8: Main: Conductance as a function of the Fermi energy for the arrangement depicted in Fig. 6. The disk radii are $r_1 = 800$ nm and $r_2 = 1000$ nm, the barrier height is $V_0 = t_0/2 = 1.35$ eV. The exponent m in Eq. (26) is specified for each dataset (solid lines). Dashed lines depict the approximating Eq. (34) for $m = 2$ with $G_{\text{Sharvin}}^{(\infty)} = 2g_0r_1|E|/(\hbar v_F)$, the asymptotic formula in Eq. (15) for $r_1/r_2 \rightarrow 1$ [thin dashed lines], and the expression following from Eq. (13) for $r_1/r_2 = 0.8$ [thick dashed line]. Inset: Conductance at $E = 100 \hbar v_F/r_1 \approx 72$ meV as a function of $L_{\text{diff}}^{(m)}/L$, with $L \equiv r_2 - r_1$, see Eq. (37). Grey solid line depicts G_{Sharvin} obtained from Eq. (31) by numerical minimization. Vertical line marks a bound on the right-hand side of Eq. (38).

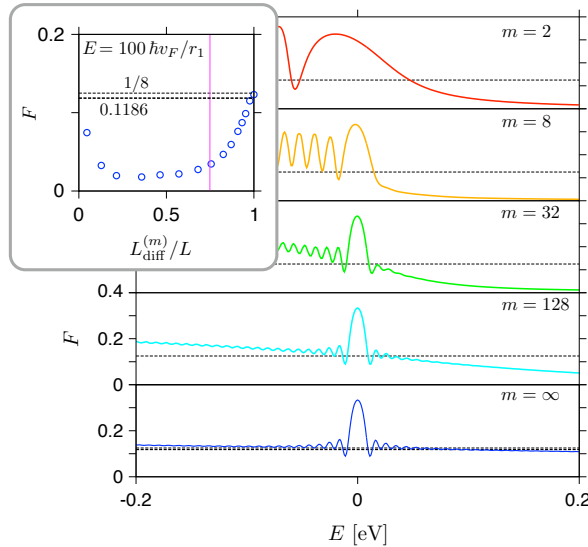


Figure 9: Fano factor as a function of the Fermi energy for the same system parameters as in Fig. 8 (solid lines). The exponent m in Eq. (26) is varied between the panels. Thin dashed line at each panel depicts the sub-Sharvin value of $F = 1/8$, see Eq. (15). Thick dashed line in the bottom panel marks the value obtained from Eq. (14) for $r_1/r_2 = 0.8$. Inset: Fano factor at $E = 100 \hbar v_F/r_1 \approx 72$ meV as a function of $L_{\text{diff}}^{(m)}$, see Eq. (37). Vertical line marks a bound on the right-hand side of Eq. (38).

Substituting $a = r_1/r_2 = 0.8$ into Eqs. (13) and (14) we

obtain, respectively,

$$G/G_{\text{Sharvin}}^{(\infty)} \approx 0.8219 \quad \text{and} \quad F \approx 0.1186. \quad (35)$$

Both predictions differ by about 5% from the asymptotic values given in Eq. (15) and corresponding to $V_0 \rightarrow \infty$, $m \rightarrow \infty$, and $r_1/r_2 \rightarrow 1$; the conductance is expected to be elevated, whereas noise is expected to be suppressed for $r_1/r_2 < 1$. Although Eqs. (13) and (14) are proposed, still as approximations, for a perfectly rectangular barrier of an infinite height, numerical results for a finite $V_0 = 1.35$ eV, and $m = \infty$ [see blue solid lines in Figs. 8 and 9], are relatively close to the predictions given in Eq. (35). This observation applies particularly for $E \sim 0.1$ eV, i.e., for $E_{\text{diff}} \ll E \ll V_0$, where

$$E_{\text{diff}} = \frac{\hbar v_F}{L} \approx 3 \text{ meV} \quad \text{for} \quad L \equiv r_2 - r_1 = 200 \text{ nm} \quad (36)$$

denotes the energy above which Sharvin conductance overrules the pseudodiffusive conductance, see Ref. [21]. Remarkably, the conductance in such a range is definitely closer to the value given in Eq. (35) than to Eq. (15).

For the Fano factor (see Fig. 9), the situation is less clear due to oscillations of the Fabry-Pérot type with an amplitude (albeit being reduced in comparison to the rectangular geometry, see Ref. [21]) exceeding the distance between the predictions given in Eqs. (15) and (35). Therefore, when looking for a finite radii-ratio effects on the shot-noise power, one should rather focus on the $r_2 \gg r_1$ range, where the predicted suppression of F , comparing Eqs. (15) and (16), is close to 15%.

A striking feature of the data presented in Figs. 8 and 9 is a systematic evolution, for $E \gg E_{\text{diff}}$, towards the values of G given by Eq. (31) and $F \approx 0$, when decreasing the value of m , i.e., tuning the potential barrier from rectangular ($m = \infty$) towards parabolic ($m = 2$) shape. (Notice that red solid line in Fig. 8, representing the results of our numerical mode-matching for $m = 2$, precisely covers dashed line marking the approximating Eq. (34) for almost the entire range of $E > 0$ presented in the plot.)

For $E < 0$, two circular p-n junctions reduce the transmission for any finite m , resulting in the suppressed conductance (see Fig. 8) and the enhanced Fano factor (see Fig. 9), with strong oscillations due to quasibound states [52].

Since the Sharvin conductance for a disk setup ($G_{\text{Sharvin}}^{(m)}$) is m -dependent, see Eqs. (31) and (32), it is worth to introduce the effective sample length evolving with m , such that $L_{\text{diff}} = r_2 - r_1$ for $m = \infty$ (rectangular barrier), and $L_{\text{diff}} \ll r_2 - r_1$ for $m = 2$ (parabolic barrier). (In the latter case, a narrow weakly-doped ring is placed near the distance of $r = r_c$ from the disk center, allowing one to understand why the approximation given in Eq. (34) works well for $E \gg E_{\text{diff}}$.) The effective length can be defined via E_{diff} (36) by imposing $V(\pm L_{\text{diff}}/2) = -E_{\text{diff}}$, leading to

$$L_{\text{diff}}^{(m)} = 2r_0 \left(\frac{\hbar v_F}{2r_0 V_0} \right)^{1/m}. \quad (37)$$

One easily finds that the above reduces to $L_{\text{diff}}^{(\infty)} = 2r_0 = r_2 - r_1 \equiv L$ for a rectangular barrier; also, we have $L_{\text{diff}}^{(2)} =$

$L\sqrt{E_{\text{diff}}/V_0} \ll L$. Subsequently, characteristic length scale of a potential jump $\Delta r = (L - L_{\text{diff}})/2$, can be compared with the Fermi wavelength $\lambda_F = 2\pi/k_F(r_c) = \hbar v_F/|E|$, allowing to expect that for $\lambda_F/2 \lesssim \Delta r$ the barrier cannot longer be regarded as rectangular. The last condition can be rewritten as

$$\frac{L_{\text{diff}}}{L} \lesssim 1 - \frac{\pi \hbar v_F}{r_0 |E|}, \quad (38)$$

giving $L_{\text{diff}}/L \lesssim 0.7487$ for $E = 100 \hbar v_F/r_1$ and the remaining parameters as used in Figs. 8 and 9.

Inset in Fig. 8, where we display the conductance for the Fermi energy fixed at $E = 100 \hbar v_F/r_1$ (such that $G_{\text{Sharvin}}^{(\infty)} = 200 g_0$) as a function of L_{diff} , unveils a clear switching behavior ruled by the inequality in Eq. (38): For L_{diff} below the upper bound, the datapoints (representing the results of numerical mode-matching for selected integer m -s) closely follow G_{Sharvin} obtained by performing the minimization in Eq. (31) [grey solid line]. For L_{diff} exceeding the bound, G shows a fast convergence to the value expected for a rectangular barrier ($m = \infty$) and given explicitly in Eq. (35).

Similarly, the Fano factor for $E = 100 \hbar v_F/r_1$ (see inset in Fig. 9) remains close to $F \approx 0$ for L_{diff} below the bound in Eq. (38); above the bound, F converges to the limiting value lying between the prediction in Eq. (35) and $F = 1/8$ [see Eq. (15) for $r_1/r_2 \rightarrow 1$]. Elevated values of F for $L_{\text{diff}}/L \lesssim 0.1$ signal a significant role of the evanescent modes (with $0 < T_j \ll 1$), which may affect the noise much stronger than the conductance; see Eq. (7).

V. A SECTION OF THE DISK WITH INFINITE-MASS BOUNDARIES

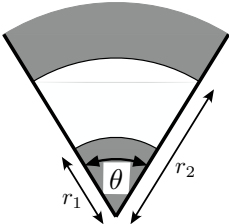


Figure 10: A section of the Corbino disk in graphene (white area) attached to heavily-doped leads (shadow areas) and bounded with infinite-mass confinement (tick lines). The opening angle $\theta = \pi/3$ and the radii ratio $r_1/r_2 = 0.5$ are set for an illustration.

Whole the derivation presented in Sec. II, in particular, the approximating formulas for the conductance and Fano factor given in Eqs. (13) and (14), can be easily extended onto a section of the disk bounded with infinite-mass confinement, as shown in Fig. 10. Since the absolute value of transverse momentum $|k_y|$ does not change after a collision with the boundary [38], key results following from the double-contact formula for incoherent transmission, see Eqs. (9) and (10), remain unaltered. For the reasons which become clear later in

this Section, one only needs to replace the value of Sharvin conductance in Eq. (13) by

$$G_{\text{Sharvin}} = \frac{\theta}{\pi} g_0 r_1 k_F, \quad (39)$$

with the opening angle $\theta < 2\pi$, the inner radii r_1 , and the Fermi momentum k_F . (Notice that we limit our considerations to the rectangular potential barrier, leading uniquely-defined k_F for the entire sample area). For the Fano factor, Eq. (14) holds true for a bounded disk section as well.

Details of the mode-matching for coherent scattering of Dirac fermions in the system of Fig. 10 are presented in Ref. [53]. Here we only recall the main formulas allowing one to determine transmission eigenvalues for a discrete set of θ -s and arbitrary dimensionless parameters $k_F r_1, r_1/r_2$.

Having in mind the solution for the full disk presented in Sec. III, we now introduce the sample edges via infinite-mass boundary conditions. After Berry and Mondragon [38], we impose that the angular current vanishes at the sample edges, namely

$$(\mathbf{j})_n = \hat{\mathbf{n}} \cdot [\Psi^\dagger (\hat{x}\sigma_x + \hat{y}\sigma_y) \Psi] = 0, \quad (40)$$

where $\hat{\mathbf{n}} = (\cos \alpha, \sin \alpha)$ is the unit vector normal to the boundary, the spinor wavefunction $\Psi = (\Psi_a, \Psi_b)^T$, and the remaining symbols are same as in Eq. (17). This leads to [54]

$$\Phi_b/\Phi_a = i \exp(i\alpha), \quad (41)$$

where $\alpha = 0$ for one edge (i.e., at $\varphi = \pi/2$) or $\alpha = \pi + \theta$ for the other (at $\varphi = \theta + \pi/2$). The solutions, being linear combinations of the form $a_j \Psi_j + b_j \Psi_{-j}$, with $\Psi_j = e^{j(j-1/2)\varphi} (\chi_a, \chi_b e^{i\varphi})^T$ again, can be found for a discrete set of opening angles $\theta \equiv \theta_l = \pi/(2l+1)$, with $l = 0, 1, 2, \dots$. Explicit formulas for wavefunctions are rather lengthy and omitted here (see Appendix A in Ref. [53] for details); instead, we summarize their basic features as follows: (i) Due to Eq. (41), the values of j contributing to charge-transfer characteristics are now restricted to

$$j = \frac{\pi(2n+1)}{2\theta}, \quad n = 0, 1, 2, \dots, \quad (42)$$

justifying the prefactor in Eq. (39). (ii) Assuming the infinite doping in the leads, Transmission probabilities can still be calculated from Eqs. (24) and (25), with the angular-momentum quantization given by the above.

The conductance and Fano factor obtained by summing over the modes [see Eq. (7); the limit of $N \rightarrow \infty$ is taken numerically] are displayed in Figs. 11 and 12. The presentation is limited to the two values of the opening angle, $\theta = \pi$ and $\theta = \pi$, as such examples (together with the full disk studied in Sec. III) are sufficient to grasp the main features introduced with the boundaries.

In Fig. 11(a) we choose the radii ratio $r_1/r_2 = 0.8$, for which the conductance in a multimode regime (results following from the mode-matching are depicted with thick solid lines) lays in a middle of the range bounded by extreme values following from Eq. for $r_1/r_2 \rightarrow 1$ and $r_1/r_2 \rightarrow 0$ (see

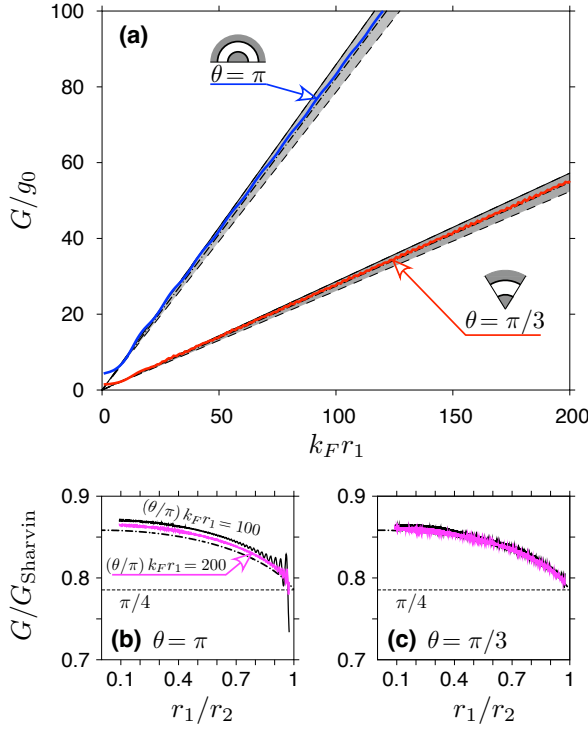


Figure 11: (a) Conductance as a function of the Fermi momentum for the system of Fig. 10 with the radii ratio $r_1/r_2 = 0.8$ and the opening angles $\theta = \pi$ (blue solid line) and $\theta = \pi/3$ (red solid line). Shaded areas mark the range between sub-Sharvin conductance ($\pi/4$) G_{Sharvin} [see Eq. (39)] (thin dashed lines) and the value of $(4 - \pi) G_{\text{Sharvin}}$ (thin solid lines) relevant for the $r_1 \ll r_2$ limit. Dashed-dotted lines correspond $G/G_{\text{Sharvin}} \approx 0.8219$ obtained from Eq. (13). (b,c) Solid lines: The conductance reduction as a function of the radii ratio for $\theta = \pi$ and $\theta = \pi/3$ for fixed values of $G_{\text{Sharvin}}/g_0 = 100$ and 200 (same in both panels). Dashed-dotted lines mark the approximating formula given by Eq. (13). The value of $G/G_{\text{Sharvin}} = \pi/4$ is marked with dashed horizontal lines.

thin dashed and solid lines, respectively), very close to the incoherent value of $G \approx 0.8219 G_{\text{Sharvin}}$ (dashed-dotted line) for $k_Fr_1 \gtrsim 100$. The corresponding values of the Fano factor in Figs. 12(a,b) are closer to $F = 1/8$ (the limit of $r_1/r_2 \rightarrow 1$ in Eq. (14)) even for noticeably higher dopings, however, a slow decay towards the value of $F \approx 0.1186$ following from Eq. (14) (dashed-dotted line) is clearly visible. Also, for both the conductance and the Fano factor displayed as functions of the radii ratio r_1/r_2 for fixed values of $G/G_{\text{Sharvin}} = (\theta/\pi) k_Fr_1$, see (respectively) Figs. 11(b,c) and Figs. 12(c,d), we observe a systematic convergence to the results following from Eqs. (13) and (14), similarly as for the full disk case in Sec. III.

It is worth to notice that a section of the disk, as depicted in Fig. 10, transforms into a rectangular sample when taking the limit of $\theta \rightarrow 0$ and $r_1/r_2 \rightarrow 1$, such that the ratio $\theta/(1 - r_1/r_2) = \text{const} \equiv W/L$. If additionally the condition for being in a multimode range, i.e., $(\theta/\pi) k_Fr_1 \gg 1$ is satisfied, one can expect, on the basis of numerical results presented here, that $G/G_{\text{Sharvin}} \rightarrow \pi/4$ and $F \rightarrow 1/8$, reproducing the

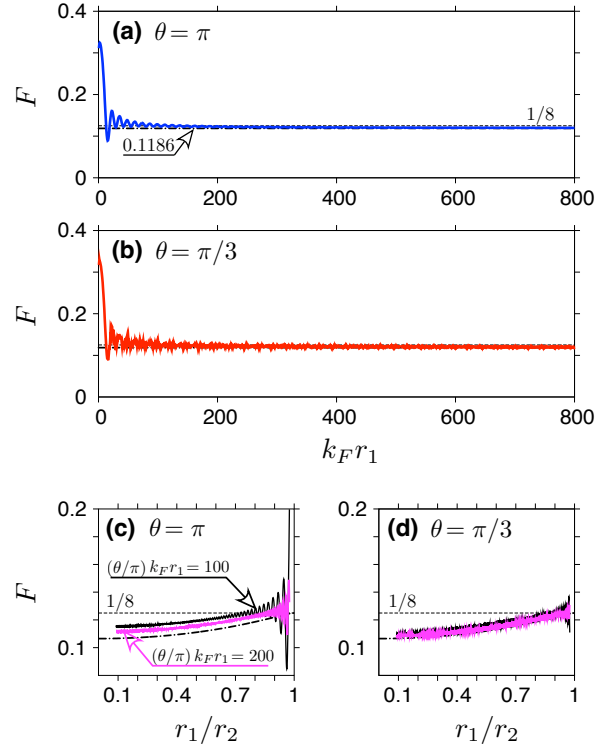


Figure 12: (a,b) Fano factor as a function of the Fermi momentum for same systems as in Fig. 11(a). The opening angle is varied between the panels. Horizontal lines show the sub-Sharvin value $F = 1/8$ (dashed) and the value following from Eq. (14) for $r_1/r_2 = 0.8$ (dashed-dotted). (c,d) Fano factor as a function of the radii ratio for same values of G_{Sharvin}/g_0 as used in Figs. 11(b,c). Dashed-dotted line depicts the formula given in Eq. (14).

values reported in Ref. [21].

What is more, the scattering in a disk section bounded with infinite-mass confinement remain independent for any j channel, with the quantization given by Eq. (42). Therefore, the transmission spectra for smooth potentials, including the examples shown in Fig. 7, will be unaffected and the crossover from the sub-Sharvin to standard Sharvin transport regime, demonstrated in Sec. IV for the full disk and in Ref. [21] for a rectangle, is predicted to appear also for a disk section.

Although the mathematics required for the mode-matching is a bit more cumbersome in the presence of infinite-mass boundaries, we see that key features of charge transport remain essentially the same as for the full disk. An issue not addressed as yet is how the results may be affected by actual (e.g., *irregular*) edges of mesoscopic samples. Large-scale simulations including possible types of disorder down to an atomic level are beyond the scope of this work; one should expect, in analogy with rectangular samples, the consistency between theoretical description presented here and experiments to appear for $\theta/(1 - r_1/r_2) \gtrsim 10$ rather than $\theta/(1 - r_1/r_2) \sim 1$, i.e., for section of narrow disks with wide opening angles. Subsequently, the verification of our predictions for the $r_1 \ll r_2$ range may only be possible using the full disk (Corbino) setup.

VI. CONCLUSIONS

The effects of sample geometry on selected charge-transfer characteristics of doped graphene nanosystems have been investigated by comparing the results for rectangular and disk-shaped (Corbino) setups with different aspect (or radii) ratios. Finite sections of the disk are also considered. Values of the conductance (G) and the Fano factor (F) obtained from analytical formulas for transmission probabilities [9, 34] are compared with results following from the proposed approximating formulas, derived by assuming incoherent scattering of Dirac fermions between two interfaces separating weakly- and heavily-doped graphene areas (i.e., electrostatically-doped sample and the leads). Numerical analysis of the scattering on a family of smooth potential barriers of a finite height, interpolating between the parabolic and the rectangular shapes, have also been carried out for the disk, supplementing our previous study for rectangular samples [21].

The results show that for rectangular samples the so-called *sub-Sharvin* transport regime, with G being directly proportional to the number of propagating modes (open channels) and $F \approx 1/8$, is entered for any aspect ratio (W/L) provided that the doping is sufficiently high, such that the Fermi wavelength (λ_F) is much shorter than either the sample width (W) or length (L). Both exact G and F show oscillations (of the Fabry-Pérot type) around mean values coinciding with the sub-Sharvin values (derived by assuming incoherent scattering), with the amplitude decreasing with increasing W/L or doping. For disk-shaped samples, as well as for disk sections, the oscillations are suppressed, since inner and outer interfaces are characterized by different curvatures corresponding to their radii, $r_1 < r_2$, and the double-contact analogy no longer applies. What is more, G and F become weakly radii-ratio dependent, with high-doping limits for thin disks ($r_1 \approx r_2$) approaching the results for rectangular samples; in the opposite ($r_1 \ll r_2$) range, the disk G is slightly enhanced (yet still smaller than the Sharvin conductance), whereas F is slightly suppressed. For smooth potentials, transport proper-

ties of familiar quantum point contacts are restored as soon as λ_F becomes comparable with the characteristic length-scale of a potential jump Δr .

These findings illustrate how peculiar transmission dependence on incident angle for weakly-doped/heavily-doped graphene interface (leading, e.g., to the Klein tunneling in case of normal incidence) may affect measurable quantities of mesoscopic graphene samples. Next to well-known Sharvin transport occurring in various ballistic structures, and pseudodiffusive charge transport in undoped graphene samples, one should also expect non-universal (geometry-dependent) reduction of G , by a factor varying from $\pi/4$ to $4 - \pi$, comparing to the Sharvin value G_{Sharvin} , and amplification of the shot-noise power (with F between $(9\pi - 28)/(12 - 3\pi) \approx 0.1065$ and $1/8$), depending on whether one or two interfaces govern the charge transport.

Since existing experimental works on various systems in graphene report either the Sharvin conductance, in case a constriction governing the transport is distant from sample-lead interfaces [43], or the values of $F \approx 1/8$ in case of a rectangular sample with long parallel interfaces [11, 12], we think it would be beneficial to confirm experimentally our predictions for an intermediate situation, i.e., when the transport is ruled by one interface and a role of the other is reduced.

Note added. — When the work was in principle complete, we became aware of experimental work on Corbino disk with radii ratio up to $r_2/r_1 \approx 4.5$ [55]. At low temperatures, conductance suppression of about 10% (compared to the Sharvin conductance) is observed, being not far from our prediction for incoherent scattering [see Eq. (13)].

Acknowledgments

We thank to Shahal Ilani for the correspondence. The work was supported by the National Science Centre of Poland (NCN) via Grant No. 2014/14/E/ST3/00256. Computations were partly performed using the PL-Grid infrastructure.

-
- [1] G. W. Semenoff, Phys. Rev. Lett. **53**, 2449 (1984).
[2] K. S. Novoselov, A. K. Geim, S. V. Morozov, D. Jiang, M. I. Katsnelson, I. V. Grigorieva, S. V. Dubonos, and A. A. Firsov, Nature **438**, 197 (2005).
[3] Y. Zhang, Y.-W. Tan, H. L. Stormer, and P. Kim, Nature **438**, 201 (2005).
[4] E. C. Peters, A. J. M. Giesbers, M. Burghard, and K. Kern, Appl. Phys. Lett. **104**, 203109 (2014).
[5] Y. Zeng, J. I. A. Li, S. A. Dietrich, O. M. Ghosh, K. Watanabe, T. Taniguchi, J. Hone, and C. R. Dean, Phys. Rev. Lett. **122**, 137701 (2019).
[6] A. B. Kuzmenko, E. van Heumen, F. Carbone, and D. van der Marel, Phys. Rev. Lett. **100**, 117401 (2008).
[7] R. R. Nair, P. Blake, A. N. Grigorenko, K. S. Novoselov, T. J. Booth, T. Stauber, N. M. R. Peres, A. K. Geim, Science **320**, 1308 (2008).
[8] M. I. Katsnelson, K. S. Novoselov, and A. K. Geim, Nature Phys. **2**, 620 (2006).
[9] J. Tworzydło, B. Trauzettel, M. Titov, A. Rycerz, and C. W. J. Beenakker, Phys. Rev. Lett. **96**, 246802 (2006).
[10] E. B. Sonin, Phys. Rev. B **77**, 233408 (2008).
[11] R. Danneau, F. Wu, M. F. Craciun, S. Russo, M. Y. Tomi, J. Salmilehto, A. F. Morpurgo, and P. J. Hakonen, Phys. Rev. Lett. **100**, 196802 (2008).
[12] A. Laitinen, G. S. Paraoanu, M. Oksanen, M. F. Craciun, S. Russo, E. Sonin, and P. Hakonen, Phys. Rev. B **93**, 115413 (2016).
[13] A. A. Balandin, S. Ghosh, W. Bao, I. Calizo, D. Teweldebrhan, F. Miao, and C. N. Lau, Nano Lett. 2008, **8**, 902 (2008).
[14] H. Yoshino and K. Murata, J. Phys. Soc. Jpn. **84**, 024601 (2015).
[15] J. Crossno, J. K. Shi, K. Wang, X. Liu, A. Harzheim, A. Lucas, S. Sachdev, P. Kim, T. Taniguchi, K. Watanabe *et al.*, Science **351**, 1058 (2016).
[16] A. N. Pal, V. Kochat, and A. Ghosh, Phys. Rev. Lett. **109**, 196601 (2012).

- [17] A. Rycerz, Phys. Rev. B **87**, 195431 (2013).
- [18] L. Huang, H. Y. Xu, C. Grebogi, and Y. C. Lai, Phys. Rep. **753**, 1 (2018).
- [19] G. S. Paraoanu, New J. Phys. **23**, 043027 (2021).
- [20] A. Rycerz, Materials **14**, 2704 (2021).
- [21] A. Rycerz and P. Witkowski, Phys. Rev. B **104**, 165413 (2021).
- [22] Yu. V. Nazarov and Ya. M. Blanter, *Quantum Transport: Introduction to Nanoscience*, (Cambridge University Press, Cambridge, UK, 2009), Chap. 1, p. 47.
- [23] Yu. V. Sharvin, Zh. Eksp. Teor. Fiz. **48**, 984 (1965) [Sov. Phys. JETP **21**, 655 (1965)].
- [24] C. W. J. Beenakker, and H. van Houten, Solid State Phys. **44**, 1 (1991).
- [25] R. Landauer, IBM J. Res. Dev. **1**, 223 (1957).
- [26] M. Büttiker, Y. Imry, R. Landauer, and S. Pinhas, Phys. Rev. B **31**, 6207 (1985).
- [27] The second condition ($k_F L \gg 1$) is required to guarantee that the contribution from evanescent modes (with $|k_y| > k_F$) is insignificant next to the contribution from propagating modes.
- [28] Y.-M. Lin, V. Perebeinos, Z. Chen, and P. Avouris, Phys. Rev. B **78**, 161409(R) (2008).
- [29] N. Tombros, A. Veligura, J. Junesch, M. H. D. Guimarães, I. J. Vera-Marun, H. T. Jonkman, and B. J. van Wees, Nature Phys. **7**, 697 (2011).
- [30] S. Ihnatsenka and G. Kirczenow, Phys. Rev. B **85**, 121407(R) (2012).
- [31] F. Libisch, S. Rotter, and J. Burgdörfer, New J. Phys. **14**, 123006 (2012).
- [32] M. Kamada, V. Gall, J. Sarkar, M. Kumar, A. Laitinen, I. Gornyi, and P. Hakonen, Phys. Rev. B **104**, 115432 (2021).
- [33] V. V. Cheianov and V. I. Fal'ko, Phys. Rev. B **74**, 041403(R) (2006).
- [34] A. Rycerz, P. Recher, and M. Wimmer, Phys. Rev. B **80**, 125417 (2009).
- [35] A. Rycerz, Phys. Rev. B **81**, 121404(R) (2010).
- [36] D. Suszalski, G. Rut, and A. Rycerz, J. Phys. Mater. **3**, 015006 (2020).
- [37] S. Datta, *Electronic Transport in Mesoscopic Systems*, (Cambridge University Press, Cambridge, UK, 1997), Chap. 3, p. 129. DOI: <https://doi.org/10.1017/CBO9780511805776>.
- [38] M. V. Berry and R. J. Mondragon, Proc. R. Soc. Lond. A **412**, 53 (1987).
- [39] For other boundary conditions, see Refs. [9, 34].
- [40] We use the identity and first derivative of the above over a ; see also I. S. Gradshteyn and I. M. Ryzhik, *Table of Integrals, Series, and Products*, Seventh Edition (Academic Press, New York, 2007), Eq. 2.553.3.
- [41] In a similar plot shown in Ref. [34] (Fig. 5) the difference between the Sharvin and the exact conductance is difficult to notice since the presentation is limited to $2k_F r_1 \leq 20$.
- [42] For an alternative derivation using the conformal mapping technique, see Ref. [34].
- [43] B. Terrés, L. Chizhova, F. Libisch *et al.*, Nat. Commun. **7**, 11528 (2016).
- [44] A. Rycerz and D. Suszalski, Phys. Rev. B **101**, 245429 (2020).
- [45] G. Giovannetti, P. A. Khomyakov, G. Brocks, V. M. Karpan, J. van den Brink, and P. J. Kelly, Phys. Rev. Lett. **101**, 026803 (2008).
- [46] T. Cusati, G. Fiori, A. Gahoi, V. Passi, M. C. Lemme, A. Fortunelli, and G. Iannaccone, Sci. Rep. **7**, 5109 (2017).
- [47] We calculated the Hankel functions, $H_\nu(x)^{(1,2)} = J_\nu(x) \pm iY_\nu(x)$ with $\nu \geq 0$, employing the double-precision regular [irregular] Bessel function of the fractional order $J_\nu(x)$ [$Y_\nu(x)$] as implemented in Gnu Scientific Library (GSL), see: <https://www.gnu.org/software/gsl/doc/html/specfunc.html#bessel-functions>. For $\nu < 0$, we use $H_{-\nu}^{(1)}(x) = e^{i\pi\nu} H_\nu^{(1)}(x)$ or $H_{-\nu}^{(2)}(x) = e^{-i\pi\nu} H_\nu^{(2)}(x)$.
- [48] Numerical integration of Eqs. (18,19) were performed utilizing a standard forth-order Runge-Kutta algorithm. A spacial step of 5 pm was sufficient to keep the unitarity error, $\max(|\epsilon_j|) < 10^{-8}$, with $\epsilon_j = |r_j|^2 + |t_j|^2 - 1$. Summation over the modes [see Eq. (7)] was terminated when $T_j < 10^{-6}$.
- [49] We use double-precision LAPACK routine zgesv, see: E. Anderson, Z. Bai, C. Bischof, S. Blackford, J. Demmel, J. Dongarra *et al.*, *LAPACK Users' Guide*, Third Edition (Society for Industrial and Applied Mathematics, Philadelphia, USA, 1999).
- [50] The difference can be expanded as $(r_{\min} - r_c)/r_0 = -\xi/2 + \mathcal{O}(\xi^2)$, with $\xi = r_0 E / (r_c V_0) \ll 1$.
- [51] E. C. Kemble, Phys. Rev. **48**, 549 (1935).
- [52] P. G. Silvestrov and K. B. Efetov, Phys. Rev. Lett. **98**, 016802 (2007).
- [53] G. Rut and A. Rycerz, Acta Phys. Polon. A **126**, A114 (2014).
- [54] The analysis is limited to the K valley. For a generalization including valleys, K and K' , see Appendix C in Ref. [36].
- [55] C. Kumar, J. Birkbeck, J. A. Sulpizio *et al.*, Nature (London) **609**, 276 (2022).

$$I(a, b) = \frac{1}{2\pi} \int_{-\pi}^{\pi} \frac{du}{a + b \cos u} = \frac{1}{\sqrt{a^2 - b^2}}, \quad \text{for } a > |b|,$$